Reconstruction of Turbulent Flows at High Reynolds Numbers Using Data Assimilation Techniques

Belligoli, Zeno; Dwight, Richard P.; Eitelberg, Georg

Important note
To cite this publication, please use the final published version (if applicable).
Please check the document version above.

Reconstruction of Turbulent Flows at High Reynolds Numbers Using Data Assimilation Techniques

Zeno Belligoli,* Richard P. Dwight,† and Georg Eitelberg‡
Delft University of Technology, 2629 HS Delft, The Netherlands

https://doi.org/10.2514/1.J059474

This paper presents two novel data assimilation (DA) techniques for reconstructing steady turbulent flows at high Reynolds numbers by introducing perturbations to the Reynolds stress tensor computed by the turbulence model of a Favre-averaged Navier–Stokes (FANS) code. These techniques minimize the least-squares difference between an experimentally measured mean flow quantity and the corresponding quantity as computed by the FANS code. The two DA methods differ from each other in the choice of the control parameters: one perturbs the eigenvalues and eigenvectors of a baseline Reynolds stress, whereas the other perturbs the components of a baseline realizable Reynolds stress such that the perturbed result is still realizable. For the optimization procedure, a gradient-based algorithm is used in combination with a discrete adjoint methodology. The DA methods are applied to high-Reynolds-number problems, and their results compared with a reference technique. The results show that the approaches developed in this work are more effective at reconstructing the turbulent flowfield than standard techniques, but are more computationally expensive due to the high dimensionality of the optimization problem. Furthermore, it appears that only small perturbations to the control parameters are necessary to obtain significant improvements over the baseline results.

Nomenclature

$\mathcal{B}(\cdot)$	=	projection operator
$\boldsymbol{b}$	=	normalized anisotropy tensor
c	=	chord length, m
c_L	=	lift coefficient
c_p	=	pressure coefficient
d	=	dimension of the problem
$\boldsymbol{d}$	=	vector of observations
E	=	total energy per unit mass, m^2/s^2
$\boldsymbol{G}$	=	random matrix with $\boldsymbol{I}$ as mean
$\boldsymbol{h}$	=	unit quaternion
$\boldsymbol{I}$	=	identity matrix
$\mathcal{J}$	=	cost function
$\hat{\mathcal{J}}$	=	error function
k	=	turbulent kinetic energy, m^2/s^2
$\boldsymbol{L}$	=	upper triangular matrix from Cholesky decomposition of $\boldsymbol{G}$
$\boldsymbol{L_R}$	=	upper triangular matrix from Cholesky decomposition of $\boldsymbol{R}$
$1(\cdot)$	=	indicator function
M_∞	=	freestream Mach number
N_d	=	number of observations
N_m	=	number of control variables
$p(\cdot)$	=	probability density function
$\boldsymbol{Q}$	=	rotation matrix
$\boldsymbol{R}$	=	Reynolds stress tensor, m^2/s^2
$\mathcal{R}(\cdot)$	=	operator representing the Reynolds-averaged Navier–Stokes equations
$\boldsymbol{S}$	=	strain rate, s^{-1}
$\boldsymbol{U}$	=	vector of state variables
$\boldsymbol{v}$	=	velocity vector, m/s
$\boldsymbol{X}$	=	eigenvector matrix
(x_B, y_B)	=	barycentric coordinates
y^+	=	dimensionless wall distance

α_∞	=	freestream angle of attack, deg
$\boldsymbol{\beta}$	=	corrective term for the turbulence production
$\Gamma(\cdot)$	=	gamma function
γ	=	under-relaxation parameter
δ	=	dispersion parameter
δ_{ij}	=	Kronecker delta
δ^{99}	=	boundary-layer thickness, m
$\boldsymbol{\epsilon}$	=	observation noise
$\boldsymbol{\theta}$	=	vector of control parameters
$\boldsymbol{\Lambda}$	=	eigenvalue matrix
λ_i	=	eigenvalue of $\boldsymbol{b}$
ν_{turb}	=	kinematic eddy viscosity, m^2/s
ρ	=	density, kg/m^3
σ_{exp}	=	observation standard deviation
σ_θ	=	control variable standard deviation
ϕ	=	rotation angle, deg
φ_i	=	eigenvalue of $\boldsymbol{R}$
ω	=	specific dissipation rate, s^{-1}

*Ph.D. Candidate, Department of Aerodynamics; z.belligoli@tudelft.nl.
†Associate Professor, Department of Aerodynamics; r.p.dwight@tudelft.nl.
‡Full Professor, Department of Aerodynamics.

I. Introduction

DESPITE the continuous growth in computational power, the routine use of direct numerical simulations (DNSs) or large-eddy simulations (LESs) in many industry applications is unfeasible due to the extremely high requirements in terms of power, memory, and time. This is why Reynolds-averaged Navier–Stokes (RANS) computer codes are still the workhorse for turbulent simulations of industrial flows. However, RANS numerical results are affected by mesh quality, iterative convergence thresholds, level of detail of the geometry, and modeling of turbulence effects. Although techniques exist for minimizing the first three types of errors, there is no straightforward way to address errors due to the modeling of turbulence.

According to Duraisamy et al. [1], these can be categorized broadly as 1) *structural* errors, essentially arising from the choice of independent variables of the turbulence model; 2) *functional* errors, due to the choice of the functional form to describe the physical processes of the independent variables; and 3) *parametric* errors, caused by the nonuniversality of the values of closure coefficients. These factors cause the result of the simulation of a specific flow condition to deviate from the truth.

Data-driven methods make use of the increasing availability of high-fidelity data (from LES, DNS, experiments) either to build predictive models that can correct turbulence-model errors [2–5], or to apply Bayesian inference [6] to compute the optimal values of parameters or variables associated with the turbulence model for a particular test case. This paper focuses on the latter topic and,

in particular, on using variational data assimilation (DA) techniques to correct functional and structural errors.

Parametric errors are the most tractable because they form a low-dimensional vector that can be recalibrated by exploiting the full capabilities of a Bayesian inversion procedure. Several studies [7–11] dealt with parametric error correction and showed that recalibration of the closure coefficients can improve RANS results. However, the effectiveness of correcting parametric errors is limited by their inability to influence more general types of error, such as functional and structural errors.

Dealing with functional and structural errors in turbulence models implies solving high-dimensional inverse problems. The most common methods to approach these types of problems are variational or Kalman filtering techniques. Dow and Wang [12,13] and Parish and Duraisamy [14] and Singh and Duraisamy [15] used variational DA to compute a corrective scalar field of the eddy viscosity and of the turbulent production term, respectively. Duraisamy et al. showed that their variational technique could work with few high-fidelity data and for high-Reynolds-number cases. Their work was extended to three-dimensional flows by He et al. [16], and used for the correction of wind-tunnel interference effects by Belligoli et al. [17]. Singh et al. [18] introduced the use of variational techniques for correcting structural errors by using the perturbations to the eigenvalues of the anisotropy tensor as control parameters. Belligoli et al. [19] extended this variational technique to include the perturbation to the anisotropy eigenvectors. In parallel, Xiao et al. [20] and Wang and Xiao [21] developed the same concept with the ensemble Kalman filter (EnKF). This technique has the advantage of providing confidence intervals on the elements of the vector of optimal control parameters, but requires mapping the control vector to a lower-dimensional space due to the high dimensionality of the inverse problem. Finally, Schmid and coworkers [22] used variational techniques to compute an optimal forcing term corresponding to the divergence of the Reynolds stress tensor. However, this methodology worked only at low Reynolds numbers because of difficulties in computing a physical initial solution to the steady Navier–Stokes equations with zero forcing at high Reynolds numbers [23].

In this paper, which is an extension of our previous work [19], we use variational DA to correct the Reynolds stress tensor approximated by a turbulence model in two different ways. In the first one, we take the perturbations to the eigenvalues and eigenvectors of the Reynolds stress tensor as control parameters. In the second case, we exploit the random matrix approach [24] to ensure the physical realizability of the Reynolds stress tensor by selecting the perturbations to the elements of the upper triangular matrix resulting from its Cholesky decomposition as control variables. We compare these methodologies with the one proposed by Parish and Duraisamy [14] and Singh and Duraisamy [15], which is taken as reference for its simplicity and efficacy. All the methods are formulated from a Bayesian perspective, and the resulting error function computing the differences between high-fidelity data and the simulations corresponds to the maximum a posteriori (MAP) estimate of the posterior distribution of the control parameters. The optimization problem is solved using a gradient-based technique with gradients computed using a discrete adjoint methodology. As validation cases, we choose high-Reynolds-number flow problems with phenomena known to be hard to reproduce with standard turbulence models, such as separation induced by an adverse pressure gradient.

This paper is structured as follows. In Sec. II we introduce the structure of a general DA problem starting from Bayes's theorem (Sec. II.A), and then we illustrate the derivation of each of the DA variants used in this work (Secs. II.B–II.D). Section III presents the results of the application of the DA methods to two test cases: one used for validation purposes (Sec. III.A) and the other for a more in-depth analysis (Sec. III.B). Finally, Sec. IV summarizes the main findings and discusses future improvements.

II. Proposed Methodology

When working with compressible flows, a density-weighted (or Favre) averaging is used, with $\tilde{A} = \overline{\rho A} / \bar{\rho}$ being the Favre-averaged

mean quantity, A'' representing the turbulent fluctuations such that an instantaneous flow variable can be written as $A = \tilde{A} + A''$, and $\overline{(\cdot)}$ and $(\cdot)'$ are the notations for Reynolds-averaged mean and fluctuating quantities, respectively. After the averaging process, a term representing the effect of turbulence on the mean flow appears. This is the Reynolds-stress tensor $R_{ij} = \widetilde{v_i'' v_j''}$, whose value in terms of averaged quantities is unknown. RANS closure models construct an approximation of this term, and eddy viscosity models based on the Boussinesq hypothesis are industry's favorite choice. These models assume that R_{ij} is linearly related to the mean rate of strain S_{ij} through a scalar turbulent viscosity ν_{turb}, i.e.,

$$R_{ij} \approx R_{ij}^{\text{ev}} = -2\nu_{\text{turb}} S_{ij} + \frac{2k}{3}\delta_{ij} \qquad (1)$$

where k is the turbulent kinetic energy, and $S_{ij} = (\partial_j \tilde{v}_i + \partial_i \tilde{v}_j)/2 - \partial_n \tilde{v}_n/3$ is the deviatoric, trace-free part of the strain rate tensor. Eddy-viscosity models introduce additional transport equations for quantities connected to ν_{turb} in order to close the system of equations. In this work, we use Menter's $k - \omega$ shear stress transport (SST) model [25], which uses transport equations for the turbulent kinetic energy and the specific dissipation rate ω.

In principle, if turbulence modeling errors were eliminated, RANS simulations could compute the *exact* values of the mean flow quantities. Hence, our aim is to develop and compare variational DA techniques that correct the errors introduced by eddy viscosity models in order to reconstruct the turbulent flowfield at a given flow condition. A variational DA uses a gradient-based algorithm to tune a vector of N_m control parameters $\boldsymbol{\theta}$ in order to minimize an error function expressed as the difference (in a certain norm) between N_d high-fidelity (e.g., from an experiment) measurements of a quantity and the same quantity as computed by a numerical simulation. The techniques presented in this paper differ from each other in the specification of the vector of control parameters used in the optimization process.

Gradient-based methods are suited for this type of high-dimensional optimization thanks to the adjoint approach [26,27], a mathematical technique that allows one to obtain the gradients of the objective function with respect to *any* number of control parameters at the cost of only one additional flow evaluation [28,29]. Thanks to the work of Albring et al. [30,31], the SU2 [32,33] CFD software comes with a discrete adjoint framework based on algorithmic differentiation that makes it possible to obtain the gradients of many objective functions with minimal source code modifications.

This work makes use of the low-memory Broyden–Fletcher–Goldfarb–Shanno (L-BFGS) [34] optimization algorithm to update the value of $\boldsymbol{\theta}$ and compute the step size of the optimization. The initial values of the control parameters are dependent on the DA methodology, but the general idea is to specify them in such a way that the result of the first optimization iteration is that of a RANS with an uncorrected turbulence model. Finally, the optimization terminates when either

$$\max(|\partial_i \mathcal{J}|) \leq 5 \cdot 10^{-5} \qquad \text{for } i = 1, \ldots, N_m$$

or

$$\frac{\mathcal{J}^q - \mathcal{J}^{q+1}}{\max\{|\mathcal{J}^q|, |\mathcal{J}^{q+1}|, 1\}} \leq 10^{-3}$$

where q is the qth optimization iteration, $\mathcal{J}$ is the objective function, $\partial_i \mathcal{J}$ is the gradient of the objective function with respect to the ith control parameter, and the value of the thresholds are specified by the user.

The results of the DA are valuable both when forecasting the behaviour of complex systems and for recalibrating numerical models for future model development. In the next section, we use a Bayesian perspective to formulate the DA problem in a general, probabilistic setting.

A. Bayesian Formulation of the Problem

Quantities $d \in \mathbb{R}^{N_d}$ measured experimentally differ from the true values of those quantities $d_{\text{true}} \in \mathbb{R}^{N_d}$ due to measurement noise, and experimental bias. We model this discrepancy statistically as

$$d = d_{\text{true}} + \varepsilon, \qquad \varepsilon \sim \mathcal{N}(0, \sigma_{\text{exp}}^2) \qquad (2)$$

where we assume zero bias, and noise to be independent, identically distributed (i.i.d.) normal random variables with known standard deviation σ_{exp} (obtained from the experimental procedure). Given some flow-state $U = [\rho, \rho v, \rho E, \rho k, \rho \omega]^\top \in \mathcal{U}$, let $\mathcal{B}: \mathcal{U} \to \mathbb{R}^{N_d}$ be a projection that extracts the measured quantities. Under most circumstances, including here, this operator will have negligible error, so that $d = \mathcal{B}(U_{\text{true}}) + \varepsilon$ is a reasonable generalization of Eq. (2) (where $U_{\text{true}} \in \mathcal{U}$ is the true state).

However, U_{true} is unknown, and approximated by solving the RANS equations including boundary-conditions

$$\mathcal{R}(\hat{U}) = 0 \qquad (3)$$

where $\hat{U} \neq U_{\text{true}}$, introducing nonnegligible modeling error. Following the seminal work of Kennedy and O'Hagan [6] and previous work in fluid dynamics [7,9], we could write

$$d = \psi(x) \cdot \mathcal{B}(\hat{U}) + \varepsilon \qquad (4)$$

where $\psi \sim \mathcal{GP}(\mu_\psi, r_\psi)$ is a Gaussian process needed to account for the errors in $\mathcal{R}(\cdot)$. A function of the spatial location x (e.g., see [8]), its mean $\mu_\psi(\cdot)$, and covariance functions $r_\psi(\cdot, \cdot)$ must be identified from the data (under some priors). This formulation allows predictions of the quantity d at unmeasured locations, but says nothing about other quantities. For example, if d are measurements of pressure, ψ represents model error in pressure and does not speak to velocity.

Therefore in this work we deviate from Kennedy and O'Hagan's formulation by moving the statistical term representing model error into the operator $\mathcal{R}$. This is logical: the source of error is within $\mathcal{R}$, and identification of this error will allow us to make predictions of unmeasured quantities. Let this discrepancy term be $\theta \in \Theta$, and modify the governing equations as

$$\mathcal{R}(U, \theta) = 0 \qquad (5)$$

By the implicit function theorem, Eq. (5) defines a function $U: \Theta \to \mathcal{U}$, so that we can construct the statistical model

$$d = d_{\text{true}} + \varepsilon = \mathcal{B}(U(\theta)) + \varepsilon \qquad (6)$$

as an alternative to Eq. (4). To complete the model, it remains to define priors on θ.

The objective of the methods presented in this work is to find the MAP estimate of θ, minimizing the difference between experimental data and simulated prediction, subject to reasonable priors on the model error. This is an inverse problem and can be formulated in a general way using Bayes's theorem:

$$p(\theta|d) \alpha p(d|\theta) p_0(\theta) \qquad (7)$$

where $p_0(\theta)$ represents available knowledge about θ in the absence of d; $p(d|\theta)$ is the likelihood that represents the probability of observing the data given a certain value of θ, modeled with Eq. (6); and $p(\theta|d)$ is the posterior probability distribution, which is the updated probability of θ informed by the data. The posterior is not a single parameter vector, but a distribution over the parameter space. Therefore, when a representative realization of control parameters must be chosen, one reasonable choice is the MAP estimate of $p(\theta|d)$. Because we assumed that the noise elements are i.i.d., the likelihood function can be written as $p(d|\theta) = p(d_1|\theta) \cdot p(d_2|\theta) \cdot \ldots p(d_N|\theta)$. Furthermore, we assumed that they are normally distributed with standard deviation σ_{exp} with mean given by $\mathcal{B}(\theta) := \mathcal{B}(U(\theta))$. Hence the likelihood is

$$p(d|\theta) = \left(\frac{1}{\sigma_{\text{exp}}\sqrt{2\pi}}\right)^{N_d} \exp\left(-\sum_{i=1}^{N_d} \frac{(\mathcal{B}(\theta)_i - d_i)^2}{2\sigma_{\text{exp}}^2}\right) \qquad (8)$$

In case of uninformative objective priors, we have that $p(\theta|d) \propto p(d|\theta)$, and the MAP estimate can be found by minimizing the negative of the exponent of the likelihood function as

$$\min_{\theta} \hat{\mathcal{J}} = \sum_{i=1}^{N_d} \frac{(\mathcal{B}(\theta)_i - d_i)^2}{2\sigma_{\text{exp}}^2} \qquad (9)$$

If, on the other hand, we choose to specify a prior probability density function (PDF) for our control parameters θ, and we assume that they are independent and normally distributed with mean given by $\theta_{j,\text{prior}}$ for $j = 1, \ldots, N_m$, and standard deviation $\sigma_{j,\theta}$, the MAP can be obtained as

$$\min_{\theta} \mathcal{J} = \sum_{i=1}^{N_d} \frac{(\mathcal{B}(\theta)_i - d_i)^2}{2\sigma_{\text{exp}}^2} + \sum_{j=1}^{N_m} \frac{(\theta_{j,\text{true}} - \theta_{j,\text{prior}})^2}{2\sigma_{j,\theta}^2} \qquad (10)$$

Hence Eq. (10) is equivalent to a least-squares regression with Tikhonov regularization, i.e., a ridge regression. The second term in Eq. (10) acts as a regularization term that penalizes departures of the parameter vector from its presumed value. For simplicity, we make use of constant prior variances, so that the objective function can be also written as

$$\min_{\theta} \mathcal{J} = \sum_{i=1}^{N_d} (\mathcal{B}(\theta)_i - d_i)^2 + \lambda \sum_{j=1}^{N_m} (\theta_{j,\text{true}} - \theta_{j,\text{prior}})^2 \qquad (11)$$

where $\lambda = \sigma_{\text{exp}}^2 / \sigma_\theta^2$ is a relaxation parameter. The methodologies presented in Secs. II.B and II.C have an objective function similar to that of Eq. (10). In general, the type of prior specified determines the form of the regularization term, thus affecting the outcome of the minimization problem. The methodology presented in Sec. II.D uses a combination of Gaussian and gamma distributions for its priors and thus will present a different form of the regularization term.

B. Turbulent Production Perturbation Method

For a general $k - \omega$ turbulence model, the structure of the transport equations for k and ω is

$$\frac{Dk}{Dt} = P_k(U) - D_k(U) + T_k(U) \qquad (12)$$

$$\frac{D\omega}{Dt} = P_\omega(U) - D_\omega(U) + T_\omega(U) \qquad (13)$$

where $P_i(U)$, $D_i(U)$, and $T_i(U)$ are the production, destruction, and cross-production terms, respectively. Following Parish and Duraisamy [14] and Singh and Duraisamy [15], a multiplicative corrective term is introduced in the turbulence model in order to correct the functional form of the model discrepancy. This is achieved by rewriting the production term in one of the transport equations, e.g., as $\beta(x) \cdot P_\omega(U)(x)$. Just like $P_\omega(U)$, β is a spatially varying scalar field defined everywhere in the domain. The corrective term can take both positive and negative values, thus being able to influence the balance of terms of the transport equation. After the discretization of the RANS equations, β becomes a high-dimensional vector, with as many elements as the mesh points. Hence, in this case $\theta = \theta_{\text{TPP}} \equiv \beta$. We take as prior $\theta_{\text{TPP}} \sim \mathcal{N}(1.0, \sigma_\beta^2 I)$ so that the objective function in Eq. (10) becomes

$$\mathcal{J} = \sum_{i=1}^{N_d} \frac{[\mathcal{B}(\theta)_i - d_i]^2}{2\sigma_{\text{exp}}^2} + \sum_{j=1}^{N_m} \frac{(\beta_j - 1.0)^2}{2\sigma_\beta^2} \qquad (14)$$

where N_d and N_m are the number of high-fidelity data and mesh points, respectively, and the value of σ_β is based on the user's knowledge of the particular problem at hand.

In practice, this technique recalibrates the balance of terms within the transport equation, thus correcting functional errors. It has been applied to a variety of test cases [16,17,19], proving to be robust and effective. This is why it is chosen as a reference for comparing the performances of the two novel techniques presented in Secs. II.C and II.D.

C. Anisotropy Tensor Perturbation Method

The correction proposed in Sec. II.B can influence the balance of terms in the turbulent transport equations. However, its range of action is constrained by the Boussinesq hypothesis, and the correction can address only functional errors. Structural errors can be tackled by directly correcting the values of the Reynolds stress tensor. To this end, it is useful to decompose R_{ij} into factors determining its amplitude, shape, and orientation [35]. The Reynolds stress tensor is a symmetric positive-semidefinite tensor and, as such, can be decomposed in an anisotropic and isotropic components as

$$R_{ij} = 2k\left(b_{ij} + \frac{\delta_{ij}}{3}\right) \tag{15}$$

where $b_{ij} = R_{ij}/2k - \delta_{ij}/3$ is the normalized anisotropy tensor, and the tilde notation has been omitted for simplicity. The symmetry of the Reynolds stress implies that b_{ij} is also symmetric and the trace of the turbulence anisotropy is zero by construction. The requirement of physical realizability imposes that R_{ij} has to be positive semidefinite, which can be expressed through constraints on the elements of b_{ij}, namely, that $b_{ij} \in [-1/3, 2/3]$ for $i = j$, and $b_{ij} \in [-1/2, 1/2]$ for $i \neq j$ [36]. In addition, the anisotropy tensor can be factored into

$$\boldsymbol{b} = \boldsymbol{X}\boldsymbol{\Lambda}\boldsymbol{X}^T \tag{16}$$

where $\boldsymbol{X}$ is a matrix whose columns are orthonormal eigenvectors, and $\boldsymbol{\Lambda}$ is the diagonal matrix of real eigenvalues such that $\lambda_1 \geq \lambda_2 \geq \lambda_3$. Because b_{ij} has zero trace, then we can write $\lambda_3 = -(\lambda_1 + \lambda_2)$. The amplitude, shape, and orientation of the Reynolds stress tensor are represented by the turbulent kinetic energy k, the turbulence anisotropy eigenvalues, and eigenvectors, respectively.

The coordinate system described by the eigenvectors is called the *principal coordinate system*, and the eigenvalues represent the magnitude of the tensor in each of the eigenvector directions. The eigenvalues of the Reynolds stress (φ_i) and those of the turbulence anisotropy (λ_i) are related via

$$\lambda_i = \frac{\varphi_i}{2k} - \frac{1}{3} \tag{17}$$

These considerations permit to describe different limiting behaviors of turbulence in relation to φ_i. One-component turbulence (only one $\varphi_i \neq 0$) indicates that turbulent fluctuations exist only along one direction. Two-component turbulence (two $\varphi_i \neq 0$) indicates that the velocity fluctuations are active in the plane formed by the principle axes associated with the nonzero φ_i. Three-component turbulence (all three $\varphi_i \neq 0$) indicates that fluctuations exist in various strengths along any direction. Finally, the plane strain state is encountered when at least one anisotropy eigenvalue λ_i is equal to zero. In this case the turbulence along the direction corresponding to that eigenvalue is due only to isotropic stress. This is the state that pertains to all Reynolds stress tensors computed with eddy viscosity turbulence models.

A powerful tool to visualize the magnitude of the anisotropy is the barycentric map proposed by Banerjee et al. [36]. This mapping leverages the fact that any realizable state of turbulence is a convex combination of its three limiting states. These can be taken to be the vertices $\{\boldsymbol{x}_{1c}, \boldsymbol{x}_{2c}, \boldsymbol{x}_{3c}\}$ of an equilateral triangle arbitrarily located in the Euclidean space. Each state of turbulence can be represented by a point $\boldsymbol{x}_B = (x_B, y_B)$ in the barycentric map as

$$x_B = C_{1c}x_{1c} + C_{2c}x_{2c} + C_{3c}x_{3c}$$
$$y_B = C_{1c}y_{1c} + C_{2c}y_{2c} + C_{3c}y_{3c}$$

with $C_{1c} = \lambda_1 - \lambda_2$, $C_{2c} = 2(\lambda_2 - \lambda_3)$, and $C_{3c} = 3\lambda_3 + 1$. The barycentric map is shown in Fig. 1. States within its boundaries are physically realizable and turbulent phenomena computed using an eddy viscosity model will have barycentric coordinates lying along the plane strain line because the Boussinesq hypothesis assumes that the effect of turbulence is proportional to the mean rate of strain. This mapping will be used to study how the proposed DA methodologies affect the characteristics of turbulence of the test cases.

To correct the Reynolds stress tensor computed with a turbulence model, we perturb the decomposed R_{ij} computed from a precursor RANS simulation as

$$R_{ij}^* = 2k^*\left(\boldsymbol{X}^*\boldsymbol{\Lambda}^*\boldsymbol{X}^{\top*} + \frac{\delta_{ij}}{3}\right) \tag{18}$$

where $k^* = k + \Delta k$, $\boldsymbol{\Lambda}^*$ is the matrix of perturbed eigenvalues, and $\boldsymbol{X}^*$ is the matrix of perturbed eigenvectors. The perturbed eigenvalues are implicitly defined through perturbations to the coordinates of the barycentric map $\boldsymbol{x}_B^* = (x_B + \Delta x_B, y_b + \Delta y_B)$. The perturbed eigenvector matrix is defined as $\boldsymbol{X}^* = \boldsymbol{Q}^*\boldsymbol{X} = (\boldsymbol{Q} + \Delta \boldsymbol{Q})\boldsymbol{X}$, where $\boldsymbol{Q}$ is a rotation matrix expressed by a combination of the elements of the unit quaternion

$$\begin{aligned}\boldsymbol{h} &= \left[\cos\frac{\phi}{2}, n_1\sin\frac{\phi}{2}, n_2\sin\frac{\phi}{2}, n_3\sin\frac{\phi}{2}\right] \\ &= \cos\frac{\phi}{2} + n_1\sin\frac{\phi}{2}\boldsymbol{i} + n_2\sin\frac{\phi}{2}\boldsymbol{j} + n_3\sin\frac{\phi}{2}\boldsymbol{k} \\ &= h_r + h_i\boldsymbol{i} + h_j\boldsymbol{j} + h_k\boldsymbol{k} \end{aligned} \tag{19}$$

Given two sets of orthonormal eigenvectors $\boldsymbol{X}$ and $\boldsymbol{X}^*$ sharing the same origin O, the Euler's rotation theorem states that there exists a unique axis of *unit* vector $\boldsymbol{n} \equiv \{n_1, n_2, n_3\}/\|\boldsymbol{n}\|$ and angle ϕ such that $\boldsymbol{X}^*$ can be obtained by rotating $\boldsymbol{X}$ by ϕ about an axis $\boldsymbol{n}$ that runs through the origin O. The rotation matrix is defined as

$$\boldsymbol{Q} = \begin{pmatrix} 1-2(h_j^2+h_k^2) & 2(h_ih_j-h_kh_r) & 2(h_ih_k+h_jh_r) \\ 2(h_ih_j+h_kh_r) & 1-2(h_i^2+h_k^2) & 2(h_jh_k-h_ih_r) \\ 2(h_ih_k-h_jh_r) & 2(h_jh_k+h_ih_r) & 1-2(h_i^2+h_j^2) \end{pmatrix} \tag{20}$$

In 2D, the only parameter needed to uniquely identify $\boldsymbol{Q}$ is the rotation angle ϕ, because any rotation can only be about the z axis
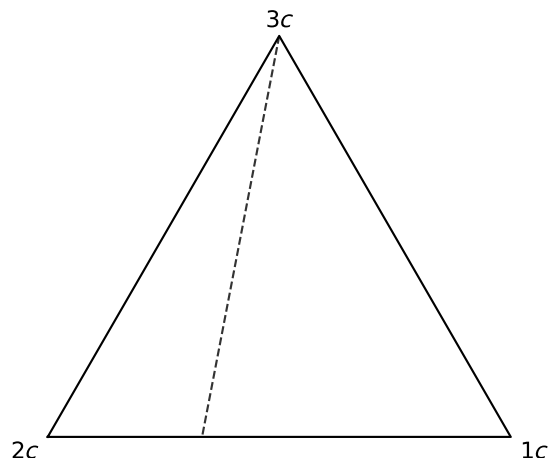

Fig. 1 The barycentric map domain. The dashed line corresponds to plane strain limit.

such that $n_1 = n_2 = 0$ and $n_3 = 1$. The baseline rotation matrix has $\phi = 0$ and thus coincides with the identity matrix, i.e., $\boldsymbol{Q} = \boldsymbol{I}$, and $\Delta \boldsymbol{Q}$ is constructed by perturbing the rotation angle and the vector components as $\phi + \Delta \phi$, $n_i + \Delta n_i$ for $i = 1, 2, 3$. Note that representing the eigenvector perturbations as a rigid body rotation automatically preserves their orthonormality. With this formulation structural errors in the modeling of turbulence can be corrected by directly assimilating perturbations to the eigenvectors and eigenvalues of the baseline Reynolds stress tensor. In practice, however, this makes the simulation difficult to converge as shown in the work of Symon et al. [23]. Hence, a turbulence model is still used for stabilizing the RANS simulation via an adaptive under-relaxation technique. This consists in expressing the Reynolds stress tensor as

$$R_{ij} \approx (1 - \gamma) R_{ij}^{ev} + \gamma R_{ij}^* \tag{21}$$

where $\gamma_n = \gamma_{\max} \min\{1, (n/n_{\max})\}$, and $n_{\max}$ is the iteration count after which γ is fixed to the value of $\gamma_{\max}$. Note that the value of the turbulent kinetic energy k in Eq. (15) could, in principle, be assimilated as well. However, in this work, it is extracted from the transport equation of the turbulence model and hence $\Delta k = 0$. Furthermore, the same Reynolds stress tensor computed in Eq. (21) is also used in the turbulent transport equations of k and ω to compute a modified production term, in line with the approach of Mishra et al. [37] and Kaandorp and Dwight [4].

In the anisotropy tensor perturbation (ATP) technique, the vector of control parameters comprehends six perturbation fields: two for the perturbation of the barycentric coordinates and four for the perturbations of the eigenvectors. Hence, the total number of control variables is six times the number of mesh points and $\boldsymbol{\theta} = \boldsymbol{\theta}_{\mathrm{ATP}} \equiv [\Delta \boldsymbol{x}_B, \Delta \boldsymbol{y}_B, \Delta \boldsymbol{\phi}, \Delta \boldsymbol{n}_1, \Delta \boldsymbol{n}_2, \Delta \boldsymbol{n}_3]^{\top}$. We assume the priors of each random field of $\boldsymbol{\theta}_{\mathrm{ATP}}$ to be $\Delta \boldsymbol{x}_B \sim \mathcal{N}(0, \sigma_{x_B}^2)$, $\Delta \boldsymbol{y}_B \sim \mathcal{N}(0, \sigma_{y_B}^2)$, $\Delta \boldsymbol{\phi} \sim \mathcal{N}(0, \sigma_{\phi}^2)$, and $\Delta \boldsymbol{n}_i \sim \mathcal{N}(0, \sigma_{n_i}^2)$ for $i = 1, 2, 3$, and we can write the objective function in Eq. (10) as

$$\mathcal{J} = \sum_{i=1}^{N_d} \frac{[\mathcal{B}(\boldsymbol{\theta})_i - d_i]^2}{2\sigma_{\exp}^2} + \sum_{j=1}^{N_m} \left[\frac{(\phi_j - 0)^2}{2\sigma_{\phi}^2} + \frac{(\Delta x_{B,j} - 0)^2}{2\sigma_{x_B}^2} \right.$$
$$\left. + \frac{(\Delta n_{1,j} - 0)^2}{2\sigma_{n_1}^2} + \frac{(\Delta n_{2,j} - 0)^2}{2\sigma_{n_2}^2} + \frac{(\Delta n_{3,j} - 0)^2}{2\sigma_{n_3}^2} \right] \tag{22}$$

which has the same structure of Eq. (14), but a different regularization term due to a different choice of design variables.

D. Random Matrix Perturbation Method

In general, a Reynolds stress tensor computed with an eddy-viscosity model may not be physically realizable [38]; i.e., its eigenvalues may lie outside of the barycentric triangle. The framework presented in Sec. II.C does not guarantee the realizability of R_{ij}, and additional constraints must be enforced for this to happen. For example, every time a point is displaced outside of the barycentric map by the perturbations to the barycentric coordinates, it could be brought back to the closest border of the triangle as discussed by Xiao et al. [20]. The ideal solution is a procedure that automatically guarantees realizability without imposing additional constraints. This is the case for the random matrix approach [24,39], which models the Reynolds stress tensor as a random matrix defined on the set $\mathbb{M}_d^{+0}$ of positive semidefinite matrices of rank $d - 1 = 2$ (we consider only the positive definite case here, because it is easily obtainable from a positive semidefinite matrix by adding a small positive quantity on its diagonal elements).

Xiao et al. [24] demonstrated that this constraint is sufficient to guarantee the realizability of each realization of the random matrix. Furthermore, it allows one to impose the minimum amount of constraints on the prior of the control parameters, thus making the DA procedure able to explore wider portions of the barycentric map. This is achieved by using the maximum entropy principle to specify the distribution of the Reynolds stress tensor, which states that, among all the PDFs mapping from $\mathbb{M}_d^{+0}$ to $\mathbb{R}^+$, the most noncommittal is the

one that satisfies all available constraints without introducing additional artificial ones. This is obtained by maximizing the entropy $S(p)$ of the PDF $p(\boldsymbol{R})$ of a random Reynolds stress tensor $[\boldsymbol{R}]$:

$$S(p) = - \int_{\mathbb{M}_d^{+0}} p(\boldsymbol{R}) \, \ell_n \, p(\boldsymbol{R}) \, \mathrm{d}\boldsymbol{R} \tag{23}$$

where $\boldsymbol{R}$ is a realization of the random Reynolds stress tensor, and we use the notation $[\cdot]$ for random matrices. For RANS turbulence modeling, the constraints that must be satisfied are as follows:

1) All realizations $\boldsymbol{R}$ must be realizable. This constraint is automatically satisfied by defining the random Reynolds stress tensor on the set $\mathbb{M}_d^{+0}$.

2) The integral of the PDF over the set must be equal to unity: $\int_{\mathbb{M}_d^{+0}} p(\boldsymbol{R}) \, \mathrm{d}\boldsymbol{R} = 1$.

In practice, it is easier to work with a normalized positive definite random matrix whose mean is the identity matrix, i.e., $\mathbb{E}\{[\boldsymbol{G}]\} = \boldsymbol{I}$. We can write

$$[\boldsymbol{R}] = \boldsymbol{L}_R^{\top} [\boldsymbol{G}] \boldsymbol{L}_R \tag{24}$$

where $\boldsymbol{L}_R$ is an upper triangular matrix with nonnegative diagonal entries obtained from the Cholesky factorization of $\boldsymbol{R}$. The PDF of $[\boldsymbol{G}]$ must also satisfy the maximum entropy principle. Taking this into consideration, and after using the Cholesky factorization such that $[\boldsymbol{G}] = [\boldsymbol{L}]^{\top} [\boldsymbol{L}]$, the following can be shown [24]:

1) The off-diagonal elements of the upper triangular random matrix $[\boldsymbol{L}]$ are $[L_{ij}] = \sigma_d w_{ij}$, with $\sigma_d = \delta \times (d + 1)^{-1/2}$, δ being a user-defined dispersion parameter such that $0 < \delta < \sqrt{2}/2$ for $d = 3$, and w_{ij} are independent Gaussian random variables with zero mean and unit variance.

2) The diagonal elements are $[L_{ii}] = \sigma_d \sqrt{2u_i}$, where u_i is a positive-valued gamma random variable with the following PDF:

$$p(u) = \mathbb{1}_{\mathbb{R}^+}(u) \frac{\zeta^{\alpha} u^{\alpha-1} \exp(-\zeta u)}{\Gamma(\alpha)} \tag{25}$$

which is the classical expression of a gamma PDF with $u, \alpha, \zeta > 0$. In the random matrix approach we have $\zeta = 1$ and $\alpha = (d + 1/2\delta^2) + (1 - i)/2$. Note that $\mathbb{1}_{\mathbb{R}^+}(u)$ is an indicator function; i.e., it is one if $u \in \mathbb{R}^+$, and zero otherwise.

The random matrix perturbation (RMP) technique uses the three diagonal and three off-diagonal elements of $[\boldsymbol{L}]$ at every mesh point as control parameters. Hence, the total number of control variables is six times the number of mesh points and $\boldsymbol{\theta} = \boldsymbol{\theta}_{\mathrm{RMP}} \equiv [\boldsymbol{L}_{11}, \boldsymbol{L}_{12}, \boldsymbol{L}_{13}, \boldsymbol{L}_{22}, \boldsymbol{L}_{23}, \boldsymbol{L}_{33}]^{\top}$. Because the prior of the diagonal elements is not Gaussian, the regularization term of the objective function does not have the structure of Eq. (10), but rather

$$\mathcal{J} = \sum_{i=1}^{N_d} \frac{(\mathcal{B}(\boldsymbol{\theta})_i - d_i)^2}{\sigma_{\exp}^2}$$
$$+ \sum_{j=1}^{N_m} \left(\frac{L_{12,j}^2 + L_{13,j}^2 + L_{23,j}^2 + L_{11,j}^2 + L_{22,j}^2 + L_{33,j}^2}{2\sigma_d^2} + \right.$$
$$\left. - \ell_n (\mathbb{1}_{\mathbb{R}_0^+}(L_{11,j}) L_{11,j}^{s_1-1} \cdot \mathbb{1}_{\mathbb{R}_0^+}(L_{22,j}) L_{22,j}^{s_2-1} \cdot \mathbb{1}_{\mathbb{R}_0^+}(L_{33,j}) L_{33,j}^{s_3-1}) \right) \tag{26}$$

where $s_i = (4/\delta^2) + 1 - i$, L_{ij} are realizations of the random variables $[L_{ij}]$, and we assumed no spatial correlation for the elements of $[\boldsymbol{L}]$. The complete derivation of the objective function can be found in Appendix A. The presence of the logarithmic term penalizes negative and small values of the diagonal terms so as to keep them positive. In this way, $\boldsymbol{G}$ will be positive definite and so will $\boldsymbol{R}$, thus automatically making it realizable, without the need to impose additional constraints as for the ATP method.

III.   Results

In this section, the DA techniques proposed in Sec. II are applied to reconstruct the flow of cases for which eddy viscosity models are known to perform poorly. These are the flow over an S809 airfoil at high angle of attack, and the separated flow behind a wall-mounted hump. The first case was used by Singh and Duraisamy [15] and Singh et al. [40] in their work and it was chosen to validate the novel methods presented in this paper. The second test case is part of the *NASA Turbulence Modeling Resource* database [41], and it is known to be challenging for eddy viscosity turbulence models. While the frameworks presented in this work can be used with different types of high-fidelity data (e.g., velocity, pressure, skin friction), we choose to use only surface pressure data because these are one of the most common types of data obtainable from experiments. This choice also allows us to observe to what extent the DA frameworks of this study can correct unobserved quantities not used in the objective function, such as the velocity field.

A.   High-Angle-of-Attack Flow over S809 Airfoil

The S809 airfoil is commonly used for the design of the blades of horizontal-axis wind turbines and was chosen by Singh and Duraisamy [15] and Singh et al. [40] as the test case for their field-inversion machine-learning framework. Experimental data at $Re_c = 2 \times 10^6$, $M_\infty = 0.2$, and at a variety of angles of attack are available from the study of Somers [42]. In our case, we perform the inversion at the highest angle of attack of the database, i.e., $\alpha_\infty = 14.24°$, for which a large region of turbulent separation with an adverse pressure gradient is present. The same structured C-grid with approximately 5.5×10^4 points as in the work of Singh and Duraisamy [15] was used. The grid convergence index based on the separation location is approximately 2% and can be used as an estimation of the discretization error [43]. The pressure coefficient from the experiment of Somers [42] is chosen as training data for the objective function. Because extracting the data is prone to errors in proximity of regions with high gradients, only the suction pressure data in the range $0.05 < x/c < 0.8$ were used. The value of γ was set to 0.5 for both the ATP and RMP methods, $\sigma_{exp} = 10^{-2}$, and all the other standard deviations were set to unity.

Figure 2 shows the baseline and assimilated pressure coefficients over the airfoil and the optimization histories for the different methods. The baseline SST model does a poor job and overpredicts the pressure on the suction side as well as the location of the separation point. All three assimilations are capable of correcting this error and no substantial differences among them are observed. However, by looking at Table 1, which shows the values of the error function $\hat{\mathcal{J}}$, one can notice that the ATP method has the best agreement with the experimental data, followed by the turbulent production perturbation (TPP) method and the RMP method. The optimization history shows
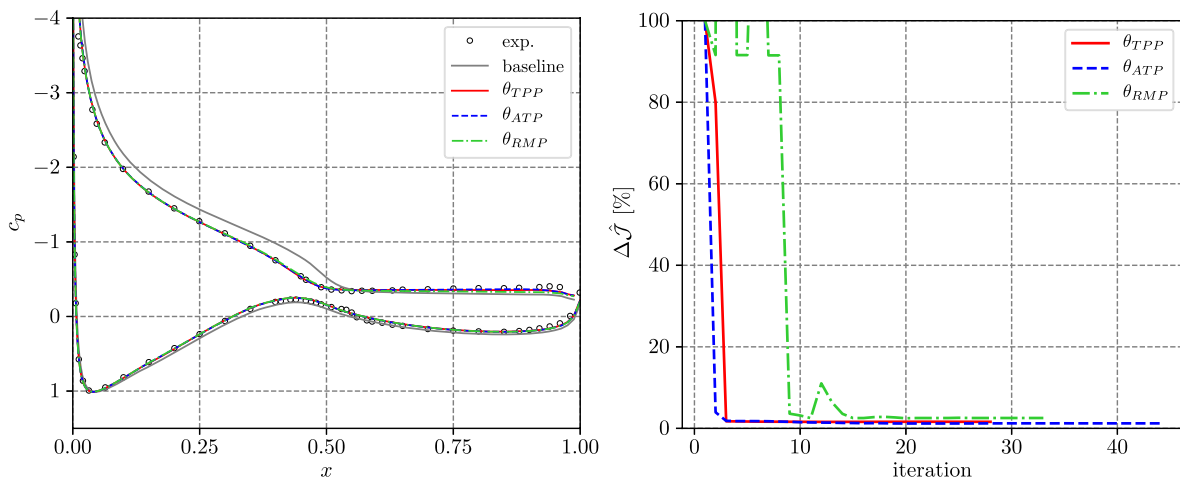
Table 1   Comparison of the value of the error function $\hat{\mathcal{J}}$, the lift coefficient c_L, the separation location x/c, and the number of optimization iterations among the baseline result and the MAP of the TPP, ATP, and RMP methods

Case	$\hat{\mathcal{J}}$	c_L	x/c	iterations
Baseline SST	1.416	1.243	0.55	——
TPP	0.0227	1.105	0.49	28
ATP	0.0163	1.108	0.50	44
RMP	0.0298	1.101	0.51	33

that the RMP method has difficulties finding a descent direction at the beginning and then has a higher final $\hat{\mathcal{J}}$ than the TPP method because the optimization converged to either a local minimum or a saddle point. This is a known problem of gradient-based optimizations, for which reaching a global optimum remains an subject of research.

Figure 3 compares the near-wall streamlines for the baseline SST model, and the TPP, ATP, and RMP methods. The size of the separation bubble is significantly larger in the results of the DA methods with respect to that of the baseline. This implies that the flows separate earlier and thus that turbulent production is decreased.

In the experiments, the separation is observed at midchord, whereas it is predicted to be at $x/c = 0.55$ by the baseline SST model. All the assimilations, on the other hand, predict the separation location to be very close to $x/c = 0.50$, as shown in the last column of Table 1. The same table also compares the posterior lift coefficients c_L, the experimental one being $c_{L,exp} = 1.083$. Once again, we observe a decisive improvement over the baseline results; hence we consider the ATP and RMP methodologies to be validated.

Figure 4 shows the perturbations to the barycentric coordinates Δx_b, Δy_b, and the unit quaternion component h_r for the ATP and RMP methods. The former two are a function of the eigenvalue perturbations, whereas the latter is a function of the eigenvector perturbations, which, for 2D cases, are given by a rotation about the axis perpendicular to the flow. The anisotropy perturbations are concentrated close to the wall and in the separated region, and are much stronger for the ATP method than the RMP method. This is in line with the fact that the RMP method has reached a different local minimum than the ATP method, due to a different, possibly rougher, topology of the optimization space. For both methods, the Δx_B perturbations tend to move the anisotropy toward the axisymmetric contraction line (i.e., the line joining the $2c$ and $3c$ corners of the barycentric map) and away from the two component limit (i.e., the line connecting the $2c$ and $1c$ corners of the barycentric map). The eigenvalue perturbations are driving the correction to the turbulence model, because the value of h_r is close to unity everywhere in the domain for both the ATP and RMP methods. The only noticeable perturbations are visible for the RMP method and are
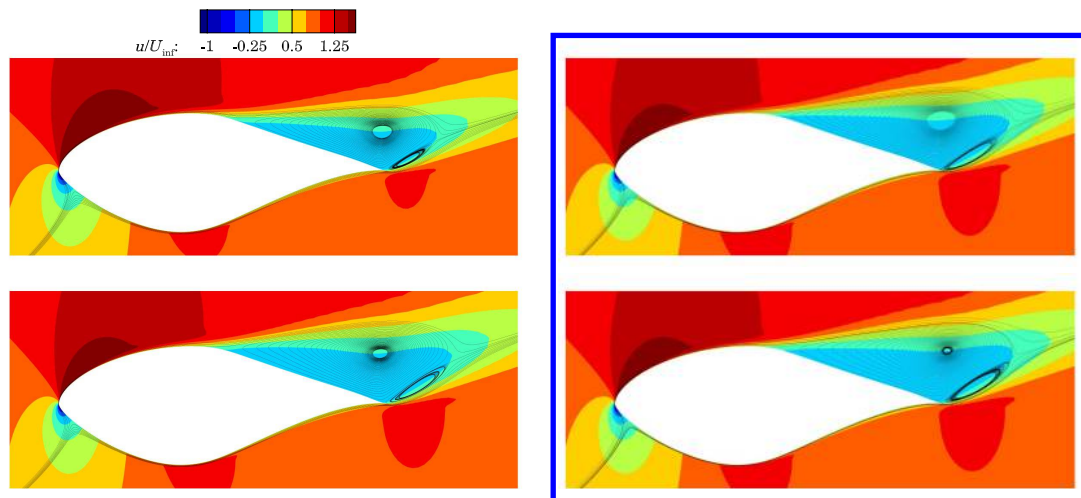

Fig. 2   Left: pressure coefficient distribution. Right: optimization history.

Fig. 3 Normalized streamwise velocity as computed by the baseline SST model (top left), the TPP (top right), the ATP (bottom left), and the RMP (bottom right) methods.
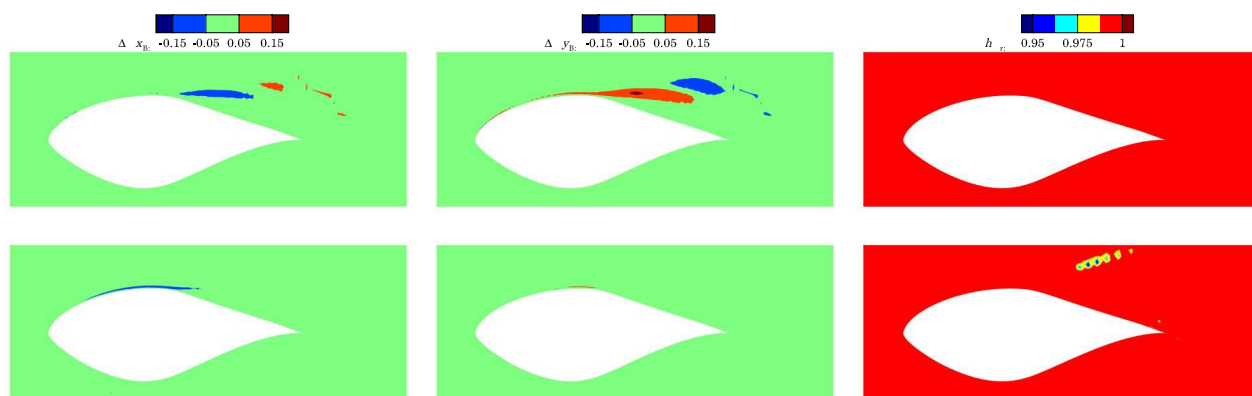

Fig. 4 Perturbations to barycentric coordinates Δx_B (left), Δy_B (middle), and h_r (right) for the ATP (top) and RMP (bottom) methods.

located at the edge of the separated region, in an area untouched by the anisotropy perturbations. For the sake of completeness, the corrective field β from the TPP method is presented in Appendix B.

B. Separated Flow Behind a Hump

The flow over a 2D hump is one of the test cases selected by NASA for the validation and verification of turbulence models. It presents separated flow behind a smooth hump protruding from a flat wall as shown in Fig. 5. Eddy viscosity turbulence models underpredict the turbulent stresses in the separated region, thus causing a too-long separation bubble. The domain consists of a rectangular channel with an inlet and an outlet, a solid bottom wall with the hump, and an upper boundary to which a symmetry boundary condition is applied. The Reynolds number based on the chord c is 9.36×10^5 and the Mach number is 0.1. The structured mesh has 4.5×10^4 points, with $y^+ \approx 0.7$. The upstream length of the channel was set to allow the natural development of the fully turbulent boundary layer in order

achieve the experimental boundary-layer thickness of $\delta^{99} = 0.0035$ m at $x/c = -2.14$ [44]. The grid convergence index based on the reattachment location is less than 1%. For the assimilation, experimental pressure coefficients on the surface of the hump in the interval $-0.8 < x/c < 2.2$ are used as training data (note that $x/c = 0$ corresponds to the hump's leading edge). The value of $\sigma_{\exp}$ is set to 10^{-3} as specified in the experiment of Greenblatt et al. [44], whereas all the other standard deviations are set to unity.

The surface pressure coefficient c_p over the hump of the three DAs is shown in Fig. 6. The baseline SST model overpredicts the pressure trough at $x/c \approx 1.3$. This is a known issue with eddy viscosity models in presence of separated flow. All DA methods significantly improve the baseline results, with the ATP and RMP methods showing an almost perfect agreement with the reference. In particular, we highlight their ability to capture subtle features such as the pressure kinks at $x/c = 0.5$ and $x/c = 1.2$. The TPP method obtains better results than the baseline but not as good as the two methods presented in this
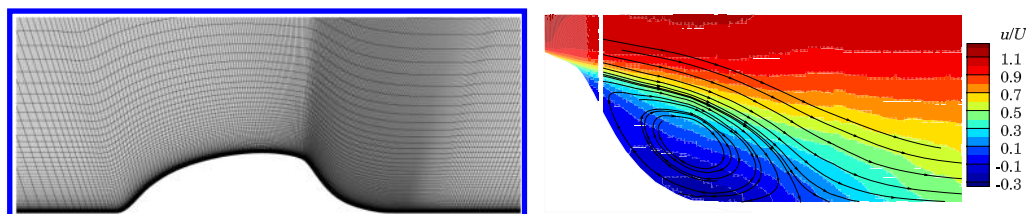

Fig. 5 Close-up of the mesh in proximity of the hump (left) and the streamwise velocity field obtained from PIV [45] (right).
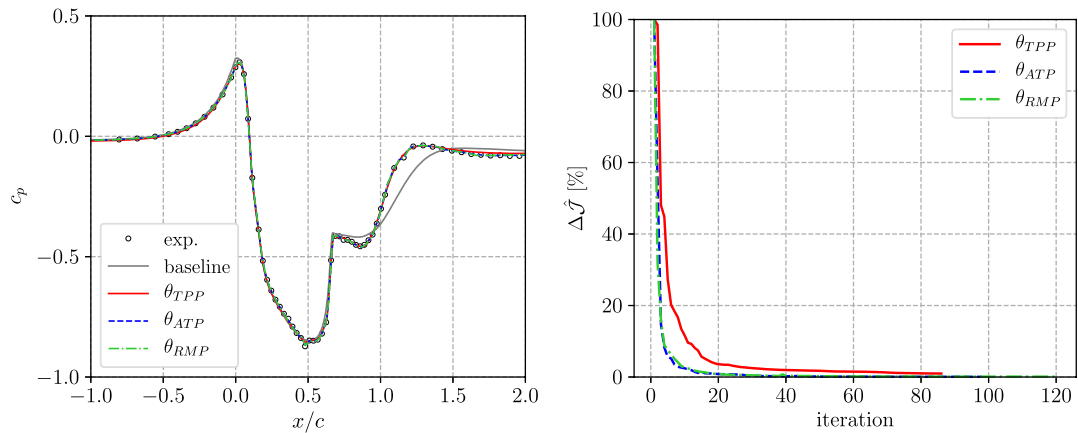
Fig. 6 Left: Pressure coefficient over the hump as computed by the TPP, ATP, and RMP methods. Right: Optimization history as a percentage reduction with respect to the initial value of $\hat{\mathcal{J}}$.
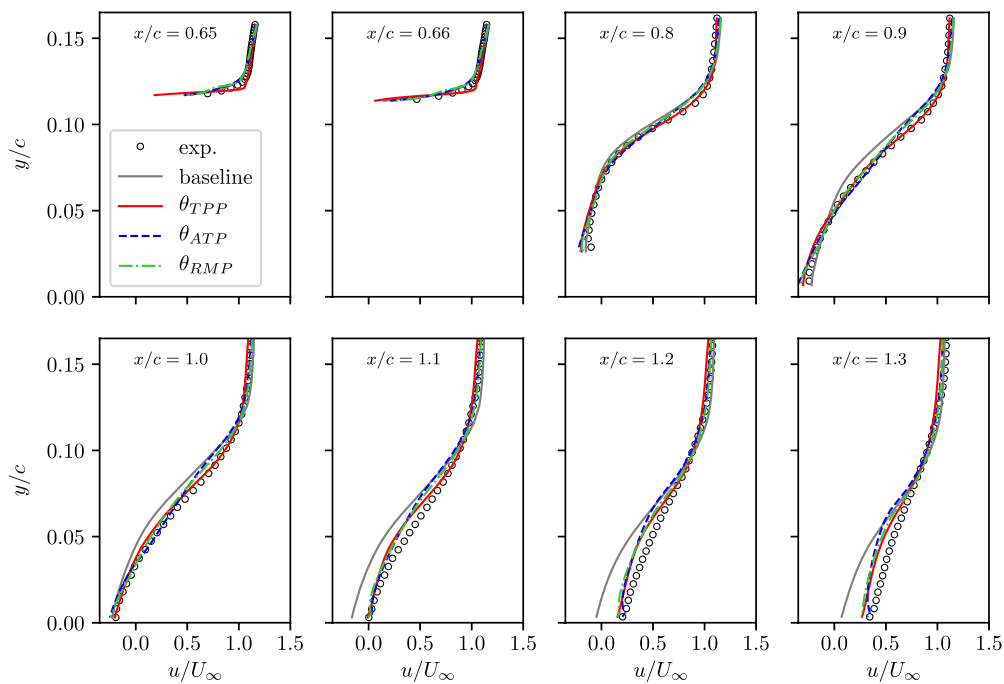

Fig. 7   Streamwise velocity profiles in the separation bubble.

work, especially downstream of the reattachment point, and in correspondence of the pressure kinks.

Figure 7 shows the normalized streamwise velocity in the separated region. The baseline model predicts too strong a reversed flow after $x/c = 1.0$, which causes a large separation region. All the DAs do a better job, in particular for $x/c > 0.9$. The ATP and RMP methods predict similar velocity profiles, with excellent agreement for $y/c > 0.10$, although they predict a slower streamwise velocity in the central part of the region $0.05 \leq y/c \leq 0.10$, where the TPP method is slightly more accurate. In any case, the differences among the DA methods are very small as shown in Table 2, whereas the

improvement over the baseline is evident. This result also demonstrates that it is sometimes possible to use only high-fidelity pressure data to better predict unobserved quantities such as the velocity.

Figure 8 shows that, for the ATP and RMP methods, the anisotropy perturbations are concentrated in the recirculation region behind the hump and persist downstream of it in the wake of the flow. The ATP method is capable of stronger perturbations to Δx_B and Δy_B than the RMP method, although they are quantitatively similar. On the other hand, no significant perturbations to h_r can be observed for both methods, thus suggesting that, for this particular test case, the eigenvector orientations remain aligned with the mean rate of strain and do

Table 2   Root-mean-square error between the CFD velocity profiles of Fig. 7 and the experimental data at several x/c locations

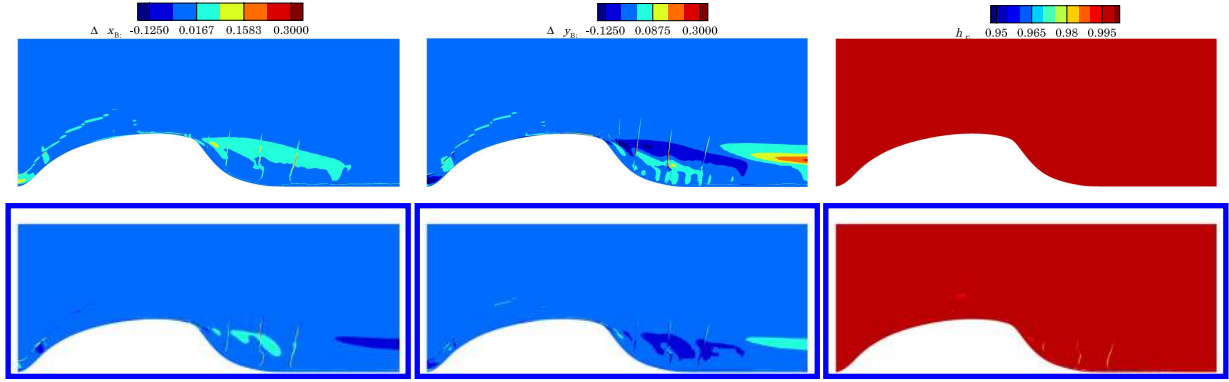| Case	$x/c = 0.65$	$x/c = 0.66$	$x/c = 0.8$	$x/c = 0.9$	$x/c = 1.0$	$x/c = 1.1$	$x/c = 1.2$	$x/c = 1.3$
Baseline	0.0403	0.0547	0.0555	0.0779	0.0955	0.1352	0.1516	0.1502
TPP	0.0869	0.0877	0.0336	0.0239	0.0328	0.0532	0.0581	0.0667
ATP	0.0494	0.0524	0.0475	0.0489	0.0467	0.0642	0.0696	0.0842
RMP	0.0551	0.0566	0.0430	0.0397	0.0413	0.0568	0.0638	0.0752

Fig. 8   Perturbations to barycentric coordinates Δx_B (left), Δy_B (middle), and h_r (right) for the ATP (top) and RMP (bottom) methods.
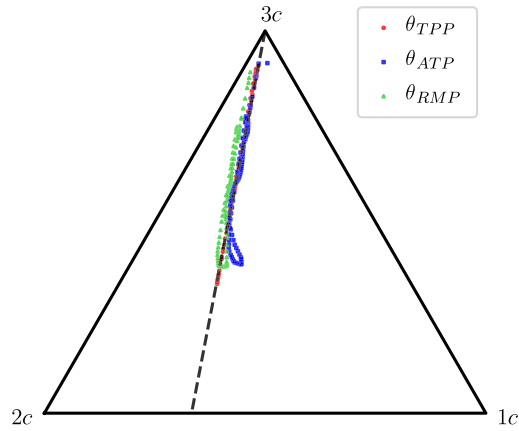

Fig. 9   Barycentric map of R_{ij} extracted along a vertical line at $x/c = 0.8$ in the interval $0 < y/c < 1.4$.

not play a significant role in correcting the errors of the turbulence model.

Figure 9 shows the barycentric map of the points extracted along a vertical line at $x/c = 0.8$. The Reynolds stress tensor was computed using Eq. (21) with $\gamma = 0.5$ for the RMP and ATP methods, and $\gamma = 0$ for the TPP method. Both the ATP and RMP methods perturb the barycentric coordinates of the sampled points away from the plane strain line, toward the $1c$ corner. In addition, the RMP method translates all the points to the left of the plane strain line, away from the $1c$ corner. It is interesting to note that the perturbations from the baseline, i.e., the distance of the ATP and RMP barycentric coordinates from the plane strain line, are relatively small. Nonetheless, they are sufficient to generate a Reynolds stress tensor capable of

dramatically improving the agreement with the high-fidelity data as shown in Fig. 6. This suggests that it could be sufficient to explore a neighborhood of the plane strain line to significantly improve eddy viscosity models, at least for 2D flow problems.

In principle, the ATP and RMP techniques can perturb the points in the barycentric triangle in the same way. This, however, does not happen, most likely due to different solution-space topologies of the two optimization problems, which cause the optimized result to lay in two different local minima.

Figure 10 shows the normalized streamwise velocity field in proximity of the hump. The results of the three DAs are qualitatively similar, as they all have a smaller recirculation region immediately behind the hump than the baseline case, with approximately the same size of the one obtained from PIV data shown in Fig. 5.

Table 3 shows the values of the error function $\tilde{\mathcal{J}}$, the streamwise location of the reattachment point, and the number of optimization iterations required to compute the MAP. It is evident that using DA techniques to correct the errors due to turbulence models is an effective strategy, and the ATP and RMP methods do a better job than the TPP because they are not subject to the limitations of the eddy viscosity hypothesis. In the experiments, the recirculation region extended to $x/c = 1.11 \pm 0.003$, and the DAs are all capable predicting this characteristics more accurately than the baseline by reducing the size of the recirculation bubble.

Furthermore, Tables 1 and 3 show that the number of optimization iterations necessary to meet the stopping criteria for the ATP and RMP methods is higher than for the TPP method. On the other hand, the time per iteration of the ATP and RMP methods is practically the same of that of the TPP method, because only few additional products of 3×3 matrices are needed for their implementation.

In conclusion, we observed how DA techniques are effective for reconstructing the flowfield of a particular test case by correcting the errors due to the turbulence model. In particular, the ATP and RMP methods have a better agreement with the high-fidelity pressure data
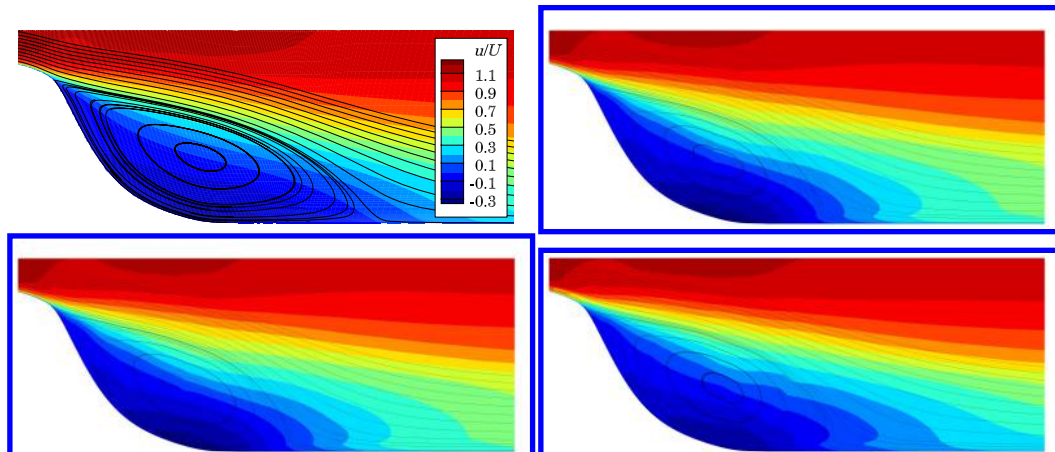

Fig. 10   Normalized streamwise velocity behind the hump as computed by the baseline SST model (top left), the TPP (top right), the ATP (bottom left), and the RMP (bottom right) methods.

Table 3 Comparison of the value of the error function $\hat{\mathcal{J}}$, the separation location x/c, and the number of optimization iterations among the baseline result and the MAP of the TPP, ATP, and RMP methods

Case	$\hat{\mathcal{J}}$	x/c	Iterations
Baseline SST	0.8897	1.26	——
TPP	0.0086	1.12	85
ATP	0.0005	1.13	99
RMP	0.0011	1.15	121

used in the objective function than the TPP method used as reference. All the methodologies tested were also able to correct unobserved quantities such as the velocity field, the extent of the recirculation region, and the location of the reattachment point.

IV. Conclusions

This paper presented two novel variational DA frameworks for the reconstruction of turbulent flowfields by correcting functional and structural errors introduced by eddy viscosity turbulence models. The two approaches differ from each other in the choice of control parameters: the ATP method uses the eigenvalues and eigenvectors of the normalized anisotropy tensor, whereas the RMP method uses the components of a positive-definite random matrix that ensures realizability of the Reynolds stress tensor. Two high-Reynolds-number flow cases known to be hard to simulate with eddy viscosity models were chosen for testing. The ATP and RMP methods showed substantial improvements with respect to the results of a baseline simulation, and comparable or better performance than a state-of-the-art variational DA technique used as reference. In particular, the ATP and RMP frameworks were able to reconstruct extremely well the high-fidelity pressure data used in the objective function, and largely improve the reconstruction of unobserved quantities such as the velocity field, the location of reattachment, and the size of the separation bubble. Furthermore, only small perturbations to the control parameters were necessary to achieve considerable improvements over the baseline results, and correcting the eigenvector orientations does not seem to have a decisive influence on improving the reconstruction of the flowfield. The ATP and RMP methods are, however, computationally more expensive than the reference DA technique considered due to a sixfold increase in the number of control parameters.

Appendix A: Derivation of the RMP Objective Function

To fulfill the maximum entropy principle, the random matrix approach requires the specifications of nonnormal priors [24]. In our case, we are interested in specifying the priors of the upper triangular matrix $[L]$ obtained from the Cholesky factorization of $[G]$. At this point, we assume that these six random vectors are statistically independent, which means that their PDFs have the following property:

$$p(L_{ij}) = p(L_{11}, L_{12}, L_{13}, L_{22}, L_{23}, L_{33})$$
$$= p(L_{11}) \cdot p(L_{12}) \cdot p(L_{13}) \cdot p(L_{22}) \cdot p(L_{23}) \cdot p(L_{33}) \quad (A1)$$

hence we can write, for a single point in the mesh,

$$p(L_{ij}|\boldsymbol{d}) \propto p(\boldsymbol{d}|L_{ij})p(L_{ij})$$
$$= p(\boldsymbol{d}|L_{ij}) \cdot p(L_{11}) \cdot p(L_{12}) \cdot p(L_{13}) \cdot p(L_{22}) \cdot p(L_{23}) \cdot p(L_{33})$$
$$\quad (A2)$$

which implies that we can independently specify the probability distribution of each element of $[L]$. Therefore, all we have to do is derive the expressions of $p(L_{ij})$ from those for w_{ij} and u_i.

A. Off-Diagonal Elements

We saw that $[L_{ij}] = \sigma_d w_{ij}$ with $w_{ij} \sim \mathcal{N}(0,1)$. For a family of normal distributions, if $X \sim \mathcal{N}(\mu, \sigma^2)$ and $Y = aX + b$, with $a, b \in \mathbb{R}$, then $Y \sim \mathcal{N}(a\mu + b, a^2\sigma^2)$. Hence, in this case we have $[L_{ij}] \sim \mathcal{N}(0, \sigma_d^2)$, and therefore

$$p(L_{ij}) \propto \exp\left(-\frac{(L_{ij})^2}{2\sigma_d^2}\right) \quad (A3)$$

B. Diagonal Elements

We want to obtain the PDF of $[L_{ii}] = \sigma_d\sqrt{2u_i}$, with u_i being a gamma random variable (RV). For gamma RVs, if $X \sim \Gamma(\alpha, \zeta)$, then $cX \sim \Gamma(\alpha, (\zeta/c))$, with $\alpha, \zeta, c > 0$. Hence $2u_i \sim \Gamma(\alpha, (1/2)) = \Gamma(\alpha, (\zeta/2))$.

Furthermore, it holds that if $X \sim \Gamma(\alpha, \zeta)$, then $X^q \sim GG(r, s, t)$ with $r = (1/\zeta)^q$, $s = (\alpha/q)$, and $t = (1/q)$, with $GG(r, s, t)$ being a generalized gamma distribution. The generalized gamma distribution is a continuous probability distribution with three parameters, and

$$p(x; r, s, t) = \mathbb{1}_{\mathbb{R}_0^+}(x)\frac{tx^{s-1}\exp(-(x/r)^t)}{r^s\Gamma(s/t)} \quad (A4)$$

Hence, in our case,

$$\sqrt{2u_i} \sim GG\left(\sqrt{\frac{2}{\zeta}}, 2\alpha, 2\right) \quad (A5)$$

Finally, for any probability distribution it holds that if $Y = g(X) = kX$ is the transformation from $\mathcal{X} = \{x|x > 0\}$ to $\mathcal{Y} = \{y|y > 0\}$, with inverse $X = g^{-1}(Y) = (Y/k)$ and Jacobian $(dX/dY) = (1/k)$, then the probability distribution of Y is

$$p_y(y) = p_x(x)\left|\frac{dx}{dy}\right| = p_x(g^{-1}(y))\left|\frac{dx}{dy}\right| \quad (A6)$$

In our case we have

$$= \sigma_d\sqrt{2u_i} \sim GG\left(\frac{y}{\sigma_d}; r, s, t\right)\left|\frac{1}{\sigma_d}\right| = \frac{ty^{s-1}\exp(-(y/\sigma_d r)^t)}{r^t\sigma_d^{(s-1)}\Gamma(s/t)}\left|\frac{1}{\sigma_d}\right|$$
$$= \frac{ty^{s-1}\exp(-(y/\sigma_d r)^t)}{(r\sigma_d)^s\Gamma(s/t)} = GG(y; r\sigma_d, s, t) \quad (A7)$$

We have the following expressions for r, s, t:

$$r = \sqrt{\frac{2}{\zeta}} = \sqrt{2}$$
$$s_i = 2\alpha = 2\left(\frac{d+1}{2\delta^2} + \frac{1-i}{2}\right)$$
$$= \frac{d+1}{\delta^2} + 1 - i = \frac{4}{\delta^2} + 1 - i$$
$$t = 2 \quad (A8)$$

Hence we can write out the full expression for $p(L_{ii})$:

$$p(L_{ii}) = \mathbb{1}_{\mathbb{R}_0^+}\frac{2L_{ii}^{(4/\delta^2)-i}\exp\left(-(L_{ii}/\sqrt{2}\sigma_d)^2\right)}{(\sqrt{2}\sigma_d)^{(4/\delta^2)+1-i}\Gamma(s/2)} \quad (A9)$$

The Gamma function is defined as $\Gamma(z) = \int_0^\infty x^{z-1}e^{-x}\,dx$ and can be easily approximated once the value of z is fixed. To fix the value of z, we need to fix s, which implies choosing a value for the dispersion parameter δ.

C. Expression of the Objective Function

These modifications have an effect on the expression of the objective function that is derived as the MAP of the posterior PDF.

$$p(x|d) \propto p(d|x)p(x) = \exp\left[-\sum_{i=1}^{N_d}\frac{(\mathcal{B}(\theta)_i - d_i)^2}{2\sigma_{\text{exp}}^2}\right] \cdot \prod_{j=1}^{N_m} p(L_{11,j})p(L_{12,j})p(L_{13,j})p(L_{22,j})p(L_{23,j})p(L_{33,j})$$

$$= \exp\left[-\sum_{i=1}^{N_d}\frac{(\mathcal{B}(\theta)_i - d_i)^2}{2\sigma_{\text{exp}}^2}\right] \cdot \prod_{j=1}^{N_m}\left[\exp\left(-\frac{L_{12,j}^2}{2\sigma_d^2}\right) \cdot \exp\left(-\frac{L_{13,j}^2}{2\sigma_d^2}\right) \cdot \exp\left(-\frac{L_{23,j}^2}{2\sigma_d^2}\right) \cdot p(L_{11,j})p(L_{22,j})p(L_{33,j})\right]$$

$$= \exp\left[-\sum_{i=1}^{N_d}\frac{[\mathcal{B}(\theta)_i - d_i]^2}{2\sigma_{\text{exp}}^2}\right] \cdot \exp\left[-\sum_{j=1}^{N_m}\frac{L_{12,j}^2 + L_{13,j}^2 + L_{23,j}^2}{2\sigma_d^2}\right] \cdot \prod_{j=1}^{N_m}[p(L_{11,j})p(L_{22,j})p(L_{33,j})]$$

$$= \exp\left[-\sum_{i=1}^{N_d}\frac{(\mathcal{B}(\theta)_i - d_i)^2}{2\sigma_{\text{exp}}^2} - \sum_{j=1}^{N_m}\frac{L_{12,j}^2 + L_{13,j}^2 + L_{23,j}^2}{2\sigma_d^2}\right] \cdot \prod_{n=1}^{3}\prod_{j=1}^{N_m}\frac{2 \cdot \mathbb{1}_{\mathbb{R}_0^+}(L_{nn,j}) \cdot L_{nn,j}^{s_n-1}\exp[-(L_{nn,j}/\sigma_d r)^2]}{(r\sigma_d)^{s_n}\Gamma(s_n/2)}$$

$$= \exp\left[-\sum_{i=1}^{N_d}\frac{(\mathcal{B}(\theta)_i - d_i)^2}{2\sigma_{\text{exp}}^2} - \sum_{j=1}^{N_m}\frac{L_{12,j}^2 + L_{13,j}^2 + L_{23,j}^2}{2\sigma_d^2}\right] \cdot \prod_{j=1}^{N_m}2^3\exp\left[-\frac{L_{11,j}^2 + L_{22,j}^2 + L_{33,j}^2}{(\sigma_d r)^2}\right] \cdot \prod_{n=1}^{3}\prod_{j=1}^{N_m}\frac{\mathbb{1}_{\mathbb{R}_0^+}(L_{nn,j}) \cdot L_{nn,j}^{s_n-1}}{(r\sigma_d)^{s_n}\Gamma(s_n/2)}$$

$$= (2^3)^{N_m} \cdot \exp\left[-\sum_{i=1}^{N_d}\frac{(\mathcal{B}(\theta)_i - d_i)^2}{2\sigma_{\text{exp}}^2} - \sum_{j=1}^{N_m}\frac{L_{12,j}^2 + L_{13,j}^2 + L_{23,j}^2}{2\sigma_d^2} - \sum_{j=1}^{N_m}\frac{L_{11,j}^2 + L_{22,j}^2 + L_{33,j}^2}{(\sigma_d r)^2}\right] \cdot \prod_{n=1}^{3}\prod_{j=1}^{N_m}\frac{\mathbb{1}_{\mathbb{R}_0^+}(L_{nn,j}) \cdot L_{nn,j}^{s_n-1}}{(r\sigma_d)^{s_n}\Gamma(s_n/2)}$$

The MAP estimate is obtained by maximizing the log of the posterior PDF. Because we are interested in a minimization problem, our objective function is the negative of the logarithm of the posterior:

$$\mathcal{J} = -\ln(p(x|d)) = -\ln(2^{3N_m}) + \sum_{i=1}^{N_d}\frac{(\mathcal{B}(\theta)_i - d_i)^2}{2\sigma_{\text{exp}}^2}$$
$$+ \sum_{j=1}^{N_m}\frac{L_{12,j}^2 + L_{13,j}^2 + L_{23,j}^2}{2\sigma_d^2} + \sum_{j=1}^{N_m}\frac{L_{11,j}^2 + L_{22,j}^2 + L_{33,j}^2}{(\sigma_d r)^2}$$
$$+ -\sum_{j=1}^{N_m}\ln\left(\prod_{n=1}^{3}\frac{\mathbb{1}_{\mathbb{R}_0^+}(L_{nn,j}) \cdot L_{nn,j}^{s_n-1}}{(r\sigma_d)^{s_n}\Gamma\left(\frac{s_n}{2}\right)}\right)$$

with $\sigma_d = \delta \times (d+1)^{-1/2} = (\delta/2)$, and δ being a user-specified dispersion parameter such that $0 < \delta < \sqrt{2}/2$ for $d = 3$; $r = \sqrt{2}$, $s_i = (4/\delta^2) + 1 - i$, and we used the logarithmic property $\ln(a \cdot b) = \ln(a) + \ln(b)$ for deriving the above expressions. Constant terms do not influence the location of the optima, and hence the objective function can be simplified to Eq. (26).

Appendix B: Corrective Field from TPP Method

Figure B1 shows the corrective field β obtained by using the TPP DA methodology. The results for the s809 airfoil show a thin region close to the surface where $\beta > 1$, thus indicating that Menter's SST turbulence model underpredicts the turbulent dissipation. As a consequence, the flow remains attached to the airfoil for longer, and this

is the reason why the separation location for the baseline model is located more downstream than that of the TPP method.

In the hump test case, the corrective field is active within the separated region behind the crest of the hump, in the shear layer above the separated region, and in the wake of the flow. The corrective field increases the dissipation in the separated region, which makes the flow reattach more upstream than in the baseline case. Furthermore, we observe that the turbulence model overpredicts the turbulent dissipation and overpredicts it in the shear layer above the recirculation region and in the wake of the flow, respectively.

References

[1] Duraisamy, K., Iaccarino, G., and Xiao, H., "Turbulence Modeling in the Age of Data," *Annual Review of Fluid Mechanics*, Vol. 51, Jan. 2019, pp. 357–377.
https://doi.org/10.1146/annurev-fluid-010518-040547

[2] Ling, J., Kurzawski, A., and Templeton, J., "Reynolds Averaged Turbulence Modelling Using Deep Neural Networks with Embedded Invariance," *Journal of Fluid Mechanics*, Vol. 807, Nov. 2016, pp. 155–166.
https://doi.org/10.1017/jfm.2016.615

[3] Wu, J.-L., Sun, R., Laizet, S., and Xiao, H., "Representation of Stress Tensor Perturbations with Application in Machine-Learning-Assisted Turbulence Modeling," *Computer Methods in Applied Mechanics and Engineering*, Vol. 346, April 2019, pp. 707–726.
https://doi.org/10.1016/j.cma.2018.09.010

[4] Kaandorp, M. L., and Dwight, R. P., "Stochastic Random Forests with Invariance for RANS Turbulence Modelling," arXiv preprint arXiv:1810.08794, 2018.
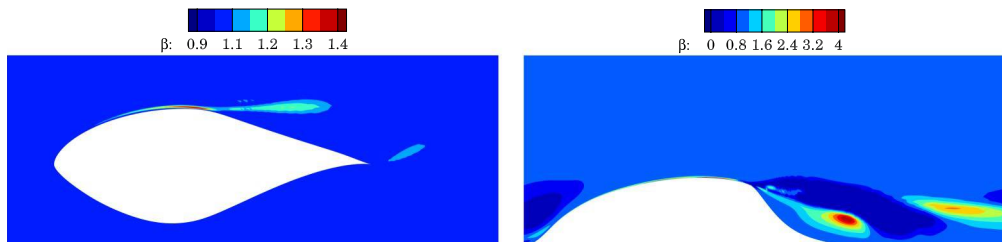
Fig. B1 Corrective field β for the s809 (left) and hump (right) cases.

[5] Schmelzer, M., Dwight, R. P., and Cinnella, P., "Machine Learning of Algebraic Stress Models Using Deterministic Symbolic Regression," arXiv preprint arXiv:1905.07510, 2019.

[6] Kennedy, M. C., and O'Hagan, A., "Bayesian Calibration of Computer Models," *Journal of the Royal Statistical Society: Series B (Statistical Methodology)*, Vol. 63, No. 3, 2001, pp. 425–464.
https://doi.org/10.1111/1467-9868.00294.

[7] Cheung, S. H., Oliver, T. A., Prudencio, E. E., Prudhomme, S., and Moser, R. D., "Bayesian Uncertainty Analysis with Applications to Turbulence Modeling," *Reliability Engineering & System Safety*, Vol. 96, No. 9, 2011, pp. 1137–1149.
https://doi.org/10.1016/j.ress.2010.09.013.

[8] Edeling, W., Cinnella, P., Dwight, R. P., and Bijl, H., "Bayesian Estimates of Parameter Variability in the k–ε Turbulence Model," *Journal of Computational Physics*, Vol. 258, Feb. 2014, pp. 73–94.
https://doi.org/10.1016/j.jcp.2013.10.027

[9] Edeling, W., Cinnella, P., and Dwight, R. P., "Predictive RANS Simulations via Bayesian Model-Scenario Averaging," *Journal of Computational Physics*, Vol. 275, Oct. 2014, pp. 65–91.
https://doi.org/10.1016/j.jcp.2014.06.052

[10] Kato, H., Yoshizawa, A., Ueno, G., and Obayashi, S., "A Data Assimilation Methodology for Reconstructing Turbulent Flows Around Aircraft," *Journal of Computational Physics*, Vol. 283, Feb. 2015, pp. 559–581.
https://doi.org/10.1016/j.jcp.2014.12.013

[11] Li, Z., Zhang, H., Bailey, S. C., Hoagg, J. B., and Martin, A., "A Data-Driven Adaptive Reynolds-Averaged Navier–Stokes k–ω Model for Turbulent Flow," *Journal of Computational Physics*, Vol. 345, Sept. 2017, pp. 111–131.
https://doi.org/10.1016/j.jcp.2017.05.009

[12] Dow, E., and Wang, Q., "Uncertainty Quantification of Structural Uncertainties in RANS Simulations of Complex Flows," *20th AIAA Computational Fluid Dynamics Conference*, AIAA Paper 2011-3865, 2011.

[13] Dow, E., and Wang, Q., "Quantification of Structural Uncertainties in the k-w Turbulence Model," *52nd AIAA/ASME/ASCE/AHS/ASC Structures, Structural Dynamics and Materials Conference*, AIAA Paper 2011-1762, 2011.

[14] Parish, E. J., and Duraisamy, K., "A Paradigm for Data-Driven Predictive Modeling Using Field Inversion and Machine Learning," *Journal of Computational Physics*, Vol. 305, Jan. 2016, pp. 758–774.
https://doi.org/10.1016/j.jcp.2015.11.012

[15] Singh, A. P., and Duraisamy, K., "Using Field Inversion to Quantify Functional Errors in Turbulence Closures," *Physics of Fluids*, Vol. 28, No. 4, 2016, Paper 045110.
https://doi.org/10.1063/1.4947045

[16] He, C., Liu, Y., and Gan, L., "A Data Assimilation Model for Turbulent Flows Using Continuous Adjoint Formulation," *Physics of Fluids*, Vol. 30, No. 10, 2018, Paper 105108.
https://doi.org/10.1063/1.5048727.

[17] Belligoli, Z., Dwight, R., and Eitelberg, G., "Assessment of a Data Assimilation Technique for Wind Tunnel Wall Interference Corrections," *AIAA SciTech 2019 Forum*, AIAA Paper 2019-0939, 2019.
https://doi.org/10.2514/6.2019-0939

[18] Singh, A. P., Duraisamy, K., and Zhang, Z. J., "Augmentation of Turbulence Models Using Field Inversion and Machine Learning," *55th AIAA Aerospace Sciences Meeting*, AIAA Paper 2017-0993, 2017.

[19] Belligoli, Z., Dwight, R., and Eitelberg, G., "RANS Data Assimilation Techniques for Wind-Tunnel Wall Interference Corrections," *AIAA Aviation 2019 Forum*, AIAA Paper 2019-2976, 2019.
https://doi.org/10.2514/6.2019-2976

[20] Xiao, H., Wu, J.-L., Wang, J.-X., Sun, R., and Roy, C., "Quantifying and Reducing Model-Form Uncertainties in Reynolds-Averaged Navier–Stokes Simulations: A Data-Driven, Physics-Informed Bayesian Approach," *Journal of Computational Physics*, Vol. 324, Nov. 2016, pp. 115–136.
https://doi.org/10.1016/j.jcp.2016.07.038

[21] Wang, J.-X., and Xiao, H., "Data-Driven CFD Modeling of Turbulent Flows Through Complex Structures," *International Journal of Heat and Fluid Flow*, Vol. 62, Dec. 2016, pp. 138–149.
https://doi.org/10.1016/j.ijheatfluidflow.2016.11.007

[22] Foures, D. P., Dovetta, N., Sipp, D., and Schmid, P. J., "A Data-Assimilation Method for Reynolds-Averaged Navier–Stokes-Driven Mean Flow Reconstruction," *Journal of Fluid Mechanics*, Vol. 759, Nov. 2014, pp. 404–431.
https://doi.org/10.1017/jfm.2014.566

[23] Symon, S., Dovetta, N., McKeon, B. J., Sipp, D., and Schmid, P. J., "Data Assimilation of Mean Velocity from 2D PIV Measurements of Flow over an Idealized Airfoil," *Experiments in Fluids*, Vol. 58, No. 5, 2017, p. 61.
https://doi.org/10.1007/s00348-017-2336-8

[24] Xiao, H., Wang, J.-X., and Ghanem, R. G., "A Random Matrix Approach for Quantifying Model-Form Uncertainties in Turbulence Modeling," *Computer Methods in Applied Mechanics and Engineering*, Vol. 313, Jan. 2017, pp. 941–965.
https://doi.org/10.1016/j.cma.2016.10.025

[25] Menter, F. R., Kuntz, M., and Langtry, R., "Ten Years of Industrial Experience with the SST Turbulence Model," *Turbulence, Heat and Mass Transfer*, Vol. 4, No. 1, 2003, pp. 625–632.

[26] Giles, M. B., and Pierce, N. A., "An Introduction to the Adjoint Approach to Design," *Flow, Turbulence and Combustion*, Vol. 65, Nos. 3–4, 2000, pp. 393–415.
https://doi.org/10.1023/A:1011430410075.

[27] Pironneau, O., "On Optimum Design in Fluid Mechanics," *Journal of Fluid Mechanics*, Vol. 64, No. 1, 1974, pp. 97–110.
https://doi.org/10.1017/S0022112074002023.

[28] Dwight, R. P., and Brezillon, J., "Effect of Approximations of the Discrete Adjoint on Gradient-Based Optimization," *AIAA Journal*, Vol. 44, No. 12, 2006, pp. 3022–3031.
https://doi.org/10.2514/1.21744

[29] Peter, J. E., and Dwight, R. P., "Numerical Sensitivity Analysis for Aerodynamic Optimization: A Survey of Approaches," *Computers & Fluids*, Vol. 39, No. 3, 2010, pp. 373–391.
https://doi.org/10.1016/j.compfluid.2009.09.013

[30] Albring, T. A., Sagebaum, M., and Gauger, N. R., "Development of a Consistent Discrete Adjoint Solver in an Evolving Aerodynamic Design Framework," *16th AIAA/ISSMO Multidisciplinary Analysis and Optimization Conference*, AIAA Paper 2015-3240, 2015.
https://doi.org/10.2514/6.2015-3240

[31] Albring, T. A., Sagebaum, M., and Gauger, N. R., "Efficient Aerodynamic Design Using the Discrete Adjoint Method in SU2," *17th AIAA/ISSMO Multidisciplinary Analysis and Optimization Conference*, AIAA Paper 2016-3518, 2016.
https://doi.org/10.2514/6.2016-3518

[32] Economon, T. D., Palacios, F., Copeland, S. R., Lukaczyk, T. W., and Alonso, J. J., "SU2: An Open-Source Suite for Multiphysics Simulation and Design," *AIAA Journal*, Vol. 54, No. 3, 2016, pp. 828–846.
https://doi.org/10.2514/1.J053813

[33] Vitale, S., Gori, G., Pini, M., Guardone, A., Economon, T. D., Palacios, F., Alonso, J. J., and Colonna, P., "Extension of the SU2 Open Source CFD Code to the Simulation of Turbulent Flows of Fluids Modelled with Complex Thermophysical Laws," *22nd AIAA Computational Fluid Dynamics Conference*, AIAA Paper 2015-2760, 2015.
https://doi.org/10.2514/6.2015-2760

[34] Liu, D. C., and Nocedal, J., "On the Limited Memory BFGS Method for Large Scale Optimization," *Mathematical programming*, Vol. 45, Nos. 1–3, 1989, pp. 503–528.
https://doi.org/10.1007/BF01589116

[35] Emory, M., Larsson, J., and Iaccarino, G., "Modeling of Structural Uncertainties in Reynolds-Averaged Navier-Stokes Closures," *Physics of Fluids*, Vol. 25, No. 11, 2013, Paper 110822.
https://doi.org/10.1063/1.4824659

[36] Banerjee, S., Krahl, R., Durst, F., and Zenger, C., "Presentation of Anisotropy Properties of Turbulence, Invariants Versus Eigenvalue Approaches," *Journal of Turbulence*, Vol. 8, Jan. 2007, p. N32.
https://doi.org/10.1080/14685240701506896

[37] Mishra, A. A., Mukhopadhaya, J., Iaccarino, G., and Alonso, J., "Uncertainty Estimation Module for Turbulence Model Predictions in SU2," *AIAA Journal*, Vol. 57, No. 3, 2018, pp. 1066–1077.
https://doi.org/10.2514/1.J057187

[38] Edeling, W. N., Iaccarino, G., and Cinnella, P., "Data-Free and Data-Driven RANS Predictions with Quantified Uncertainty," *Flow, Turbulence and Combustion*, Vol. 100, No. 3, 2018, pp. 593–616.
https://doi.org/10.1007/s10494-017-9870-6

[39] Soize, C., "Random Matrix Theory for Modeling Uncertainties in Computational Mechanics," *Computer Methods in Applied Mechanics and Engineering*, Vol. 194, Nos. 12–16, 2005, pp. 1333–1366.
https://doi.org/10.1016/j.cma.2004.06.038

[40] Singh, A. P., Medida, S., and Duraisamy, K., "Machine-Learning-Augmented Predictive Modeling of Turbulent Separated Flows over Airfoils," *AIAA Journal*, Vol. 55, No. 7, 2017, pp. 2215–2227.
https://doi.org/10.2514/1.J055595

[41] Rumsey, C. L., "Recent Developments on the Turbulence Modeling Resource Website," *22nd AIAA Computational Fluid Dynamics Conference*, AIAA Paper 2015-2927, 2015.

[42] Somers, D. M., "Design and Experimental Results for the S809 Airfoil," National Renewable Energy Lab. TR NREL/SR-440-6918, Golden,

CO, 1997.
https://doi.org/10.2172/437668

[43] Roy, C., "Review of Discretization Error Estimators in Scientific Computing," *48th AIAA Aerospace Sciences Meeting Including the New Horizons Forum and Aerospace Exposition*, AIAA Paper 2010-0126, 2010.

[44] Greenblatt, D., Paschal, K. B., Yao, C. S., Harris, J., Schaeffler, N. W., and Washburn, A. E., "Experimental Investigation of Separation Control Part 1: Baseline and Steady Suction," *AIAA Journal*, Vol. 44, No. 12,

2006, pp. 2820–2830.
https://doi.org/10.2514/1.13817

[45] "Turbulence Modeling Resource," NASA, 2019, https://turbmodels.larc .nasa.gov/.

K. Taira
Associate Editor